Supplementary Material: Unveiling photon statistics with a 100-pixel photon-number-resolving detector

Risheng Cheng,[1,*] Yiyu Zhou,[1,2,*] Sihao Wang,[1] Mohan Shen,[1] Towsif Taher,[1] and Hong X. Tang[1,2,†]

[1]*Department of Electrical Engineering, Yale University, New Haven, Connecticut 06511, USA.*
[2]*Yale Quantum Institute, Yale University, New Haven, Connecticut 06511, USA.*

(Dated: June 27, 2022)

* These authors contributed equally to this work.

† Corresponding author: hong.tang@yale.edu

Supplementary Section I. — Measurement setup

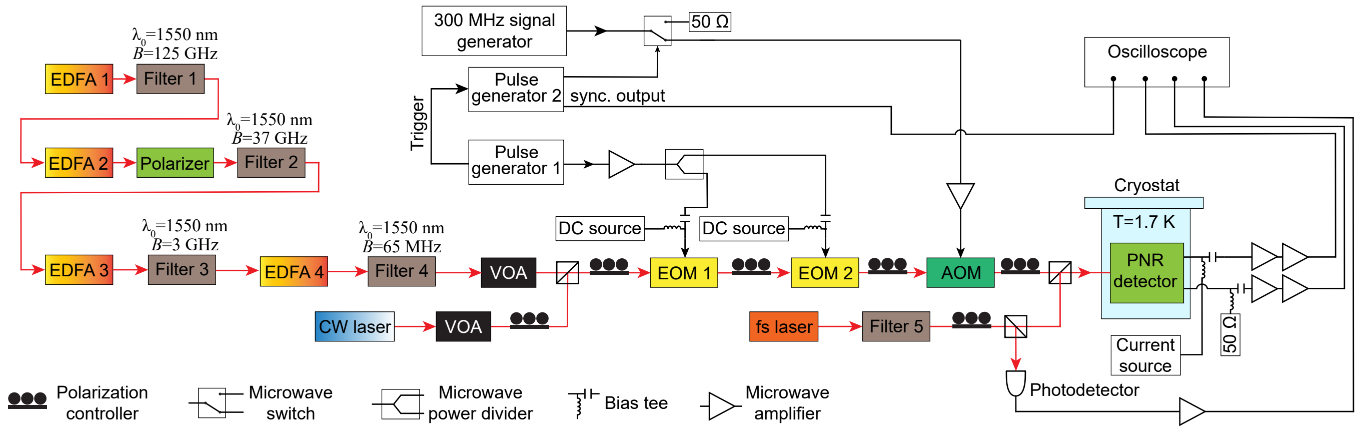

Supplementary Figure S1 | Schematic of experimental setup.

The full schematic of the measurement setup is shown in Figure S1. Four cascaded EDFAs (PriTel Inc.) along with four optical spectral filters are used to generate narrow-bandwidth thermal light with sufficient power coupled into the fiber. The four optical filters have the same central wavelength $\lambda_0 = 1550$ nm and a bandwidth of 125 GHz (Oz Optics TF-100), 37 GHz (Oz Optics TF-100), 3 GHz (Alnair Labs BVF-300CL), and 65 MHz (Micron Optics FFP-TF), respectively. Variable optical attenuators (VOAs) are employed to tune the optical power and thus the mean photon number. A continuous-wave (CW) laser (New Focus Vidia-Discrete) is used as the coherent light source. Two electro-optic modulators (EOMs, Lucent 2623NA) are used to modulate the CW light sources into pulsed sources with the pulse width down to 0.24 ns. A high-speed electrical pulse generator (Anritsu MP1763C) is used to drive the two EOMs after an RF power amplifier. An acousto-optic modulator (AOM, Gooch & Housego Fiber-Q) synced with the EOMs is employed to further increase the peak-to-background extinction ratio up to 100 dB. A 300 MHz signal generator (Hewlett Packard 8648D) is used to drive the AOM, while a pulse generator (Hewlett Packard 8161A) and a high-speed RF switch (Mini-Circuits ZASWA2-50DR-FA+) are used to tune the pulse width of the AOM. The photon-number-resolving (PNR) detector is placed in a cryostat running at the base temperature $T = 1.7$ K. A programmable source meter (Keithley 2401) is used to provide the bias current, while cascaded low-noise amplifiers (Mini-Circuits ZFL-1000LN+) are used to amplify the output RF signals from the detector. A high-speed multi-channel oscilloscope (Teledyne LeCroy HDO9404-MS) is used to digitize the output signals and count the number of pulses generated by the detector. A femtosecond (fs) laser (Toptica FemtoFiber pro IR) is used to characterize the timing jitter and map the persistence image shown in Fig. 1g of the main text. An optical filter (Oz Optics BTF-11) is used to reduce the bandwidth of the fs laser to mitigate the dispersion-induced pulse broadening. A photodetector (New Focus 1101) is used to detect the fs laser pulse, and its output is used as the trigger signal for timing jitter measurement. For the quantum discrimination experiment, we use a beam-splitter to mix the thermal light from EDFAs and the local oscillator coherent light generated by the CW laser, which results in a Laguerre statistics as discussed in the main text. For the coherent light source discrimination, we directly use the CW laser to generated the Poisson statistics after the interferometry for reduced complexity of the experiment.

Supplementary Section II. — SPICE simulation

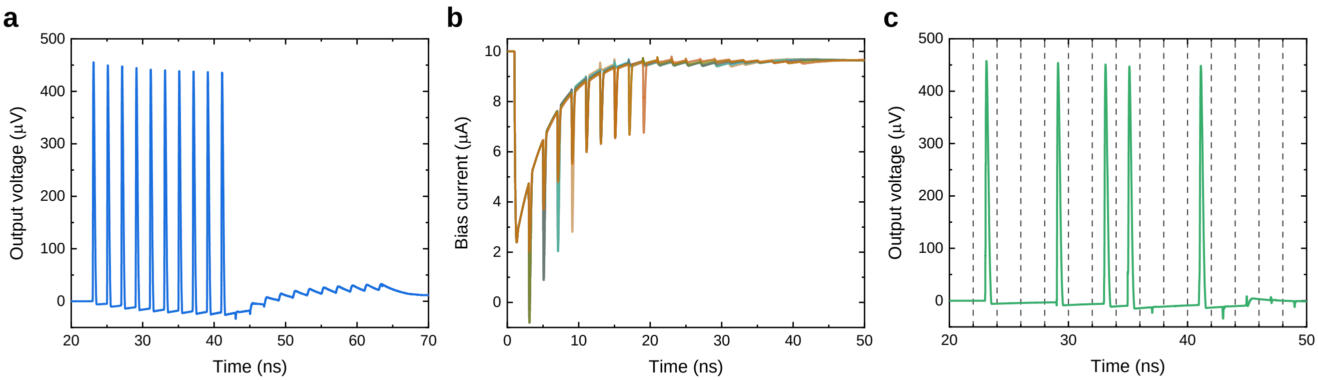

Supplementary Figure S2 | SPICE simulation results. a-b, Simulated output voltage (a) and bias currents (b) flowing through each of the nanowire detectors with all the detector pixels fired simultaneously. **c,** Simulated output voltage with a few selected detector pixels fired. The spacing between the neighboring dashed lines are 2 ns, which corresponds to the propagation time delay generated by each delay line section.

In order to confirm the operation principle, we apply a SPICE model of the SNSPD[S1] to simulate the behavior of the device after photons triggering. The modeling of the detector part is based on the electro-thermal dynamics of the superconducting nanowire that considers the evolution of the hot-spot resistance in time domain and its interaction with external circuits[S2]. The delay line sections are modeled as lossless transmission lines with a fixed delay time and characteristic impedance, while each of the impedance tapers are modeled as a series of 1,000 consecutive transmission lines with incrementally varying impedances.

Figure S2 shows the simulation results of a 10-pixel spatiotemporal-multiplexed SNSPD array. We fire all the pixels simultaneously at the time $t = 1$ ns and record the output voltage (Fig. S2(a)) as well as the bias currents flowing through each of the nanowire detectors (Fig. S2(b)). As expected, a train of pulses appear in time sequence with the spacing equal to 2 ns that is in good agreement with the delay time we set for each section of the delay lines. The minor ripples after the major pulse train are attributed to the multiple signal reflections between the detectors and the delay lines due to the slight impedance mismatch, while the slow variation of the base voltage stems from the lower cut-off frequency of the impedance taper. The tapers we use in the simulation follow the Klopfenstein design, and the total length of each tapers is equal to 20 effective wavelength of 1 GHz signal in the transmission line. We observe that longer tapers could further reduce the base voltage fluctuation, but instead it takes longer time for the fluctuation to completely subside due to the large total kinetic inductance of the device.

As shown in Fig. S2(b), the reset time of the individual detector pixels is determined by the shunted inductor and resistor, and the latching of the detectors could be avoided by appropriately choosing the inductance and resistance values. While the combination of 100 nH inductance and 20 Ω resistance is used for the simulation shown here, we observe that a wide range of the inductance (50-1000 nH) and resistance (10-200 Ω) values could be adopted for the normal functioning of the device, which guarantees a good fabrication tolerance. The multiple dips appearing during the recovery of the bias current are due to the fast output signals from neighboring fired detector pixels passing through the nanowire. We note that no significant overshoot of the currents beyond the original bias value (10 μA) is recorded, ensuring that the detectors could be biased close to their switching currents for high internal efficiency.

In Fig. S2(c), we randomly select only a few of the detector pixels to fire to mimic a more practical case. The results of the output voltage show a good on-off extinction ratio that is immune to false triggering. The rising and falling edges of the output pulses are approximately 50 ps and 400 ps, indicating the possibility of further reduction in the time bin size to increase the maximum counting rates of the detector. In addition, the fast rising edge of the signal could help maintain a good timing resolution of the detectors.

Supplementary Section III. — Device fabrication and yield

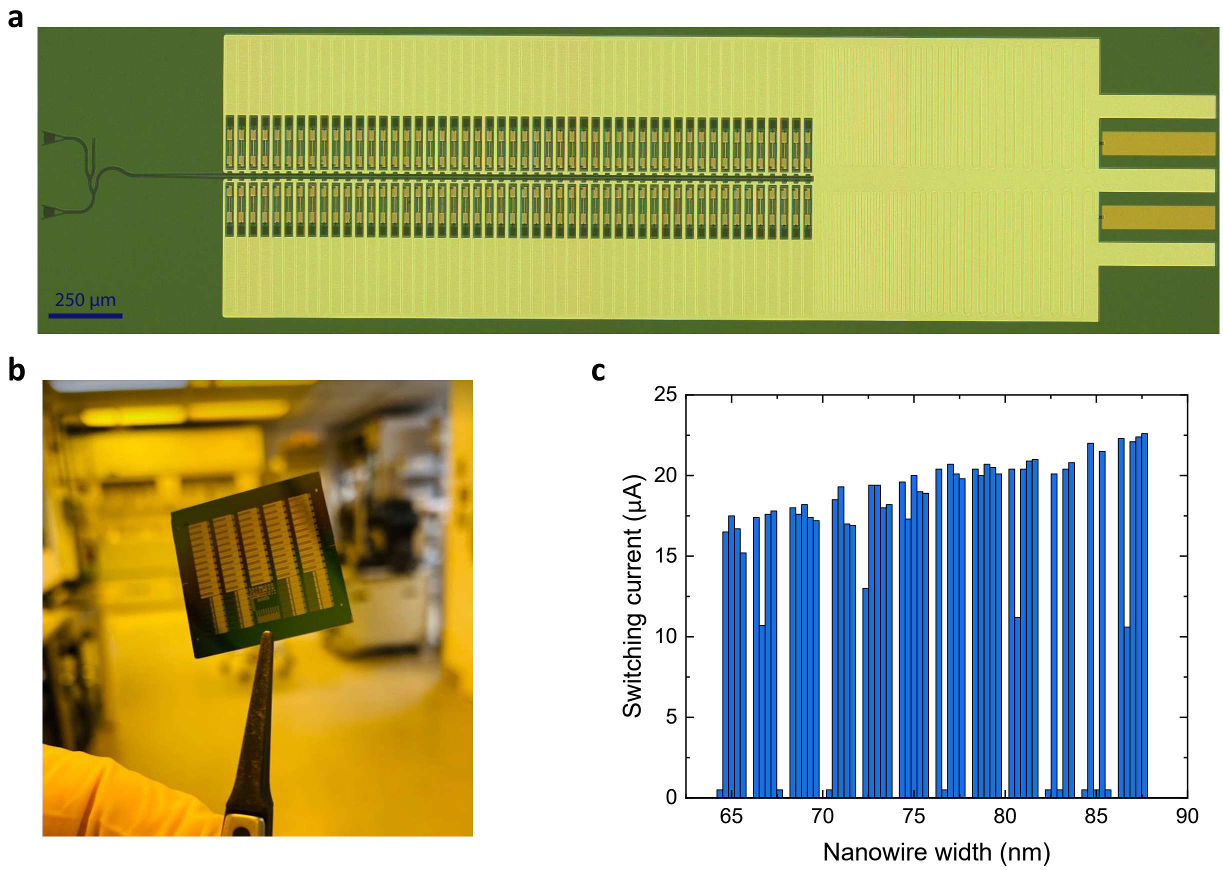

Supplementary Figure S3 | Device image and fabrication yield. a, Overview optical micrograph image of the device taken after the fabrication finished. The area of delay lines and impedance tapers are covered by alumina (AlO_x) dielectric layer and aluminum (Al) top metal ground. **b,** Photograph of the device chip. The device chip contains a total of 60 devices of 100-pixel detector, 28 devices of 16-pixel detector, and some extra test/calibration structures. They are all packed in a size of 20 mm×20 mm area. **c,** Switching currents measured for the 60 devices of 100-pixel detector array. The width of the nanowire detector is varied from 65 nm to 87 nm with the step of 2 nm, and each width include five devices with slightly different nanowire lengths.

Figure S3a shows the image of the 100-pixel detector with the area of delay lines and impedance tapers covered by alumina (AlO_x) dielectric layer and aluminum (Al) top metal ground. We have fabricated a total of 60 devices of 100-pixel detector, 28 devices of 16-pixel detector, along with some component tests and calibration structures on a single die of 20 mm × 20 mm, as shown in Fig. S3b. Among the 60 devices of 100-pixel detectors, the width of the nanowire detector is varied from 65 nm to 87 nm with the step of 2 nm, while each width include five devices with slightly different nanowire lengths to tune the absorption efficiency between each pixel. The switching currents measured for these 60 detectors are shown in Fig. S3. 51 out of 60 devices survived after fabrication, and only 4 of them demonstrate reduced switching currents, despite the large device area and a long total length of the NbN wires up to ∼400 mm. We confirm under microscope that the 9 dead devices are due to particle contamination rather than the quality of the NbN film. The results imply the high quality and uniformity of our NbN film[S3] and holds promise for further scaling our devices without performance degradation. See Methods section of the main text for more details on the fabrication method of the devices.

Supplementary Section IV. — Timing jitter

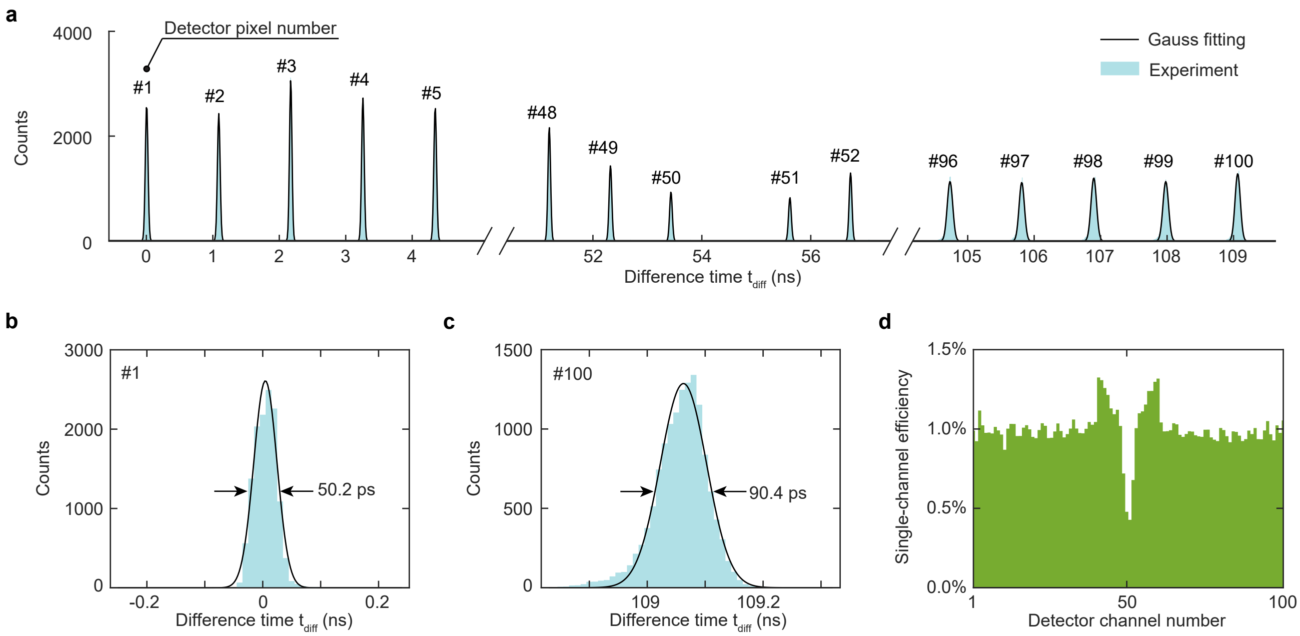

Supplementary Figure S4 | Timing jitter characterization. **a**, Histogram measured for the arrival time difference between the laser synchronization signal and the detector pulses from 100 individual pixels. The full width at half maximum (FWHM) of each peak defines the timing jitter of the corresponding detector pixel. **b-c**, Zoom-in histogram data of the 1st (b) and the 100th (c) detector pixel. **d**, Detection efficiency measured for individual 100 detector pixels.

In our experiment, we use a femtosecond laser to characterize the timing jitter of each detector pixel. A beam-splitter and photodetector are used to provide the synchronization signal of the laser, and a fast-speed oscilloscope is employed to measure and build the histogram for the arrival time difference between the synchronization signal and the pulses generated by the detector pixels. The histogram is shown in Fig. S4a, where each peak corresponds to the 100 individual pixels. The zoom-in data for the 1st and 100th pixel are also shown in Fig. S4b and c, respectively. It can be seen that the timing jitter, which is defined by the full width at half maximum (FWHM) of the histogram peak, is relatively smaller ($\sim$ 50 ps) for low pixel numbers and larger ($\sim$ 90 ps) for high pixel numbers. This is because the signals from the detector of high pixel numbers have relatively lower peak voltage, which is due to the larger ohmic loss from the top metal ground of the microwave transmission line after longer propagation (see Fig. 1g of the main text). The lower peak voltage in turn leads to lower signal-to-noise ratio and thus increase the noise-contributed jitter. In the future work, the current aluminum ground of the transmission line could be replaced by superconducting materials at the operation temperature of the device, such as niobium (Nb) or NbN, to minimize the propagation loss of the detector signals. We then calculate the total counts $C_i, i = 1, 2, \cdots, 100$ for each detector pixel by integrating the counts for each histogram peaks in Fig. S4a. The individual pixel efficiency is thus calculated by $E_i = C_i / \sum_{j=1}^{100} C_j$ and plotted in Fig. S4d. The efficiency drops significantly for the middle 49th-52nd pixels, because the nanowire detectors of these pixels are located at the end of the optical waveguide, and the absorption is limited by the finite length of the nanowires (see Fig. 1b of the main text). The uniformity of the pixel efficiencies could be further improved by better engineering of the nanowire detector length and position in the future work.

Supplementary Section V. — On-chip detection efficiency and dark count rates

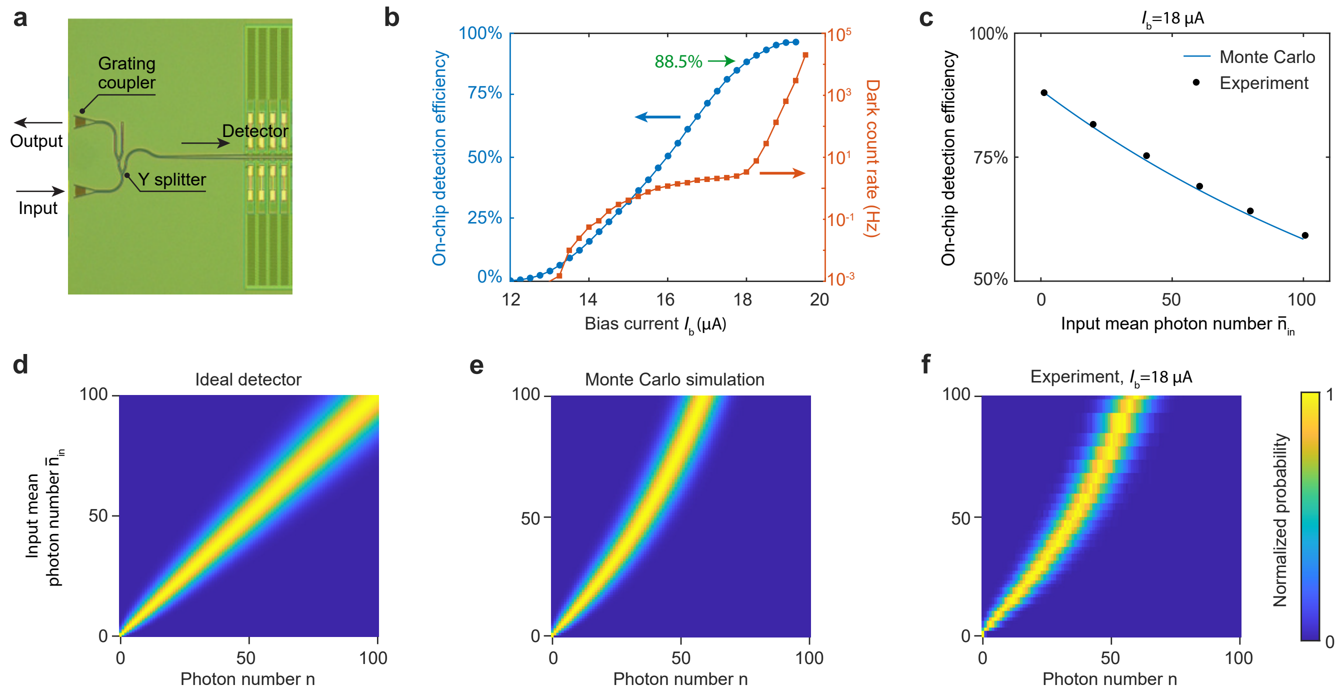

Supplementary Figure S5 | On-chip detection efficiency and dark count rates characterization. **a**, Grating coupler pair design for the measurement of on-chip detection efficiency of the device. **b**, On-chip detection efficiency and dark count rates measured as a function of the bias current I_b. **c**, On-chip detection efficiency as a function of the input mean photon number $\bar{n}_{in}$. The efficiency is measured with the bias current $I_b = 18$ μA, and the measured results agrees well with the Monte Carlo simulation results. **d**, Calculated photon number probability distribution detected by an ideal PNR detector as a function of $\bar{n}_{in}$. The ideal detector is assumed to have a 100% detection efficiency as well as an infinity number of detector pixels. **e-f**, Simulated (e) and experimentally measured (f) photon number probability distribution versus $\bar{n}_{in}$. The detector efficiency drops as $\bar{n}_{in}$ increases, as the probability of more than two photons hitting identical detector pixel increases.

We use the EDFAs and a bandwidth-tunable filter (Oz Optics BTF-11) to generate a 3 nm-bandwidth thermal light to characterize the grating coupler efficiency as well as the on-chip detection efficiency of the detector. A relatively broadband light source is used here because it has a short coherence length to mitigate the reflection-induced interference between two grating couplers. As shown in Fig. S5a, we use a symmetric design to facilitate the efficiency measurement. Here, we assume that both the grating couplers and Y-splitters are identical. The total optical transmission between the two grating couplers is measured to be $T_{\text{tot}} = 0.088\%$, and thus the fiber-to-detector transmission efficiency is $T_{\text{det}} = \sqrt{T_{\text{tot}}} = 2.97\%$. Based on this result, we can estimate the on-chip optical power and thus infer the on-chip input mean photon number $\bar{n}_{\text{in}}$ with the calibrated attenuation by the optical attenuators. The on-chip detection efficiency can then be calculated as $(\bar{n}_{\text{det}} - n_{\text{dark}})/\bar{n}_{\text{in}}$, where $\bar{n}_{\text{det}}$ and n_{dark} are the mean number of pulses detected by the PNR detector and the dark count rates, respectively. Figure S5b illustrates the measured on-chip detection efficiency and dark count rates versus the bias current I_b applied to the detector. The efficiency is measured with a relatively low input photon number $n_{in} = 1.2$ and recorded as 88.5% at the bias current of $I_b = 18$ μA, where the dark count is still at few-Hz level. The maximum efficiency reaches 95.5%, when the bias current is applied very close to the switching current ($I_{\text{SW}} = 19.5$ μA). By using thinner NbN film and narrower nanowire width, detectors can be made with wider saturation plateau in the efficiency curve[S3], and thus they can provide near-unity efficiency while operating in the regime of low dark count rate.

We also measure the detector efficiency at the fixed bias current $I_b = 18$ μA for various $\bar{n}_{\text{in}}$, as shown in Fig. S5c. The detection efficiency drops as $\bar{n}_{\text{in}}$ increases, due to the increased probability of more than two photons hitting identical pixels increases. Some of the photons are missing in this case, since each detector pixel can only output one electrical pulse for multi-photon excitation. We verify this hypothesis by performing Monte Carlo simulations, in which we model the detector with 101 pixels, and the 101st pixel is the loss channel. For a single input photon, the probability of each pixel for detecting this photon is P_i, $i = 1, 2, \cdots, 101$. Thus, we have $P_{101} = 11.5\%$ and $P_i = 0.885E_i$, where $i = 1, 2, \cdots, 100$ and E_i is the single-pixel efficiency as shown in Fig. S5d. For a single input photon, we can generate a random number $1 \leq k \leq 101$ following the probability distribution of P_i to determine which pixel will detect this photon. When the input pulse contains N photons, we generate N random numbers $k_1, k_2, \cdots, k_N$ and then count how many pixels (except the 101st pixel) are fired. As a specific example, when $N = 4$, the numerically generated random numbers are $k_1 = 4$, $k_2 = 4$, $k_3 = 5$, and $k_4 = 101$, which means that the 4th and

5th pixels are fired while one photon is annihilated due to loss. Since two pixels are fired, the detected photon number is 2. We repeat this process many times and thus we can get a probability distribution $U_{i,j=N}$ $(i = 0,1,2,\cdots)$. The value of $U_{i,j=N}$ represent the probability of detecting i photons when the input pulse contains $j = N$ photons. Obviously, we have $U_{i,j=N} = 0$ when $i > N$ and $\sum_{i=0}^{N} U_{i,j=N} = 1$. We next scan the value of j and finally arrive at a two-dimensional matrix U_{ij}. When the input pulse follows a Poisson statistics as $P_j = P_\mathrm{P}(n = j; \bar{n}_{in})$, where $\bar{n}_{in}$ is the input mean photon number, the detected photon number probability distribution can be computed as $P_\mathrm{det}(n = i) = \sum_j U_{ij} P_j$. The detected mean photon number is $\bar{n}_\mathrm{det} = \sum_n n P_\mathrm{det}(n)$, and the on-chip detection efficiency is defined as $E_\mathrm{det} = \bar{n}_\mathrm{det}/\bar{n}_\mathrm{in}$. For an ideal detector with 100% efficiency and perfect photon-number-resolving capability, we have $U_{ij} = I$, where I is the identity matrix, and the detected photon number distribution as a function of input mean photon number is shown in Fig. S5d. For our detector, we use Monte Carlo simulation to numerically compute U_{ij}, and the simulated probability distribution is shown Fig. S5e, which agrees well with our experimental data shown in Fig. S5f. The simulated on-chip detection efficiency is shown in Fig. S5c and also agrees well with the experiment.

References

[S1] K. K. Berggren, Q.-Y. Zhao, N. Abebe, M. Chen, P. Ravindran, A. McCaughan, and J. C. Bardin, "A superconducting nanowire can be modeled by using SPICE," *Supercond. Sci. Technol.* **31**, 055010 (2018).

[S2] J. Yang, A. Kerman, E. Dauler, V. Anant, K. Rosfjord, and K. Berggren, "Modeling the electrical and thermal response of superconducting nanowire single-photon detectors," *IEEE Trans. Appl. Supercond.* **17**, 581 (2007).

[S3] R. Cheng, S. Wang, and H. X. Tang, "Superconducting nanowire single-photon detectors fabricated from atomic-layer-deposited NbN," *Applied Physics Letters* **115**, 241101 (2019).